EPCM-Based Dynamic Reactive Power Planning in Renewable-Dominated Sending-End Systems

Zihan Cai
School of Electric Power
South China University of Technology
Guangzhou, China
epc_zihan@mail.scut.edu.cn

Lin Guan*
School of Electric Power
South China University of Technology
Guangzhou, China
lguan@scut.edu.cn

Yongzhe Li
School of Electric Power
South China University of Technology
Guangzhou, China
1070671983@qq.com

***Abstract*—Dynamic reactive power planning (DRPP) in renewable-dominated converter-based sending-end systems (RCSs) faces critical challenges that conventional linear models fail to capture the complex, analytically intractable converter dynamics, while high-fidelity EMT simulation is computationally prohibitive. To address this, this paper proposed an *Empirical Performance Covariance Matrix (EPCM)*-based framework for DRPP in RCSs. A comprehensive set of transient voltage and power indicators is designed to quantitatively characterize dynamic responses under reactive perturbations in RCSs. Based on these indicators, construct EPCM metric and quantitative metrics for global controllability, local voltage support, and compensator redundancy are derived. A bi-level optimization model is then formulated, where the upper level maximizes system-wide controllability and the lower level enhances weak-bus voltage support while coordinating multi-device interactions. Case studies on a 16 GW PV–VSC–HVDC system demonstrate that the proposed compensator configuration achieves faster voltage recovery, lower overvoltage peaks, and smoother post-fault power restoration compared with conventional sensitivity-based approaches. The results confirm that the EPCM-based framework effectively enhances both global and local voltage stability in large-scale RCSs.**

***Index Terms*—dynamic reactive power planning, renewable-dominated converter-based sending-end system, transient performance indicators, empirical performance covariance matrix.**

I. Introduction

As the global pursuit of clean and low-carbon energy intensifies, the large-scale development of renewable generation has become a defining direction of energy system transformation. In western and northern China, vast desert and Gobi regions offer abundant renewable resources, presenting both opportunities and challenges for large-scale development. These regions are characterized by vast renewable clusters, limited local load demand, and weak grid infrastructure, with most of the generated power transmitted to distant load centers via high-voltage direct current (HVDC) systems. In this context, a representative configuration of a RCS has emerged, where large-scale Grid Following (GFL) Renewable units are interconnected through multi-level AC networks and integrated into remote Grid-forming (GFM) voltage source converter(VSC) stations for long-distance HVDC power delivery [1] [2].

This type of system exhibits stability characteristics fundamentally different from those of conventional grids. In the absence of synchronous generators, the system lacks both inertia support and voltage stiffness [3] [4], leaving the frequency and voltage references eentirely dependeent on the GFM VSC-HVDC station. The combined dominance of renewable generation and power electronic converters renders the system highly susceptible to voltage instability. Under steady-state conditions, renewable power fluctuations often exceed the regulation capability of static compensators. Their discrete switching and slow response limit effectiveness in dynamic regulation. During transient disturbances, the active-reactive coupling and complex control mode transitions of converters cause overvoltage and post-fault oscillations [5] [6], distinct from the conventional undervoltage problem in synchronous grids. Consequently, RCSs exhibit weak voltage regulation and insufficient reactive power absorption, necessitating new evaluation frameworks and fast-responding dynamic reactive power compensation devices such as STATCOMs to ensure secure operation.

In RCS, DRPP faces major challenges in analytically representing the complex transient interactions among converters. Conventional linearization-based methods [7], rely on simplified algebraic formulations around specific operating points and therefore fail to capture the broadband dynamics and control-loop interactions that dominate RCS behavior. Dynamic linearization techniques, including trajectory sensitivity analysis [8], can represent time-varying dynamics but remain insufficient for describing mode switching and nonlinearities introduced by control limits. To address these limitations, several studies have integrated electromagnetic transient (EMT) simulations into heuristic optimization frameworks [9]. However, repeated EMT evaluations lead to a combinatorial explosion in the search space, rendering computationally prohibitive.

To address these limitations, data-driven modeling has emerged as an effective alternative for DRPP. Leveraging high-fidelity simulation data, such methods capture the nonlinear dynamics and multi-timescale interactions of RCS without explicit analytical models of converter controls. Among them, the *Empirical Controllability Covariance (ECC)* quantifies voltage controllability by statistically analyzing system responses to small perturbations or EMT-based injections [10], thereby establishing a data-driven framework for dynamic voltage characterization in complex power systems.

However, the ECC framework faces two intrinsic challenges in large-scale RCS. First, constructing state covariance matrices from full time-domain trajectories produces excessive data and computational burden, while redundant information from non-critical buses obscures the key states governing instability. Moreover, during transients, dynamic var compensators at different buses exhibit synergistic and redundant effects, and even adverse control interactions may arise. Therefore, dynamic reactive power siting requires more effective indicators

This work is supported by the Smart Grid-National Science and Technology Major Project of China (2025ZD0804900) and the National Natural Science Foundation of China (U22B6007).

979-8-3315-8138-1

to evaluate the overall voltage stability impact of multi-point configurations.

To overcome these limitations, this paper proposes an EPCM–based framework for DRPP in RCS. The EPCM reconstructs ECC-derived controllability information within a compact, physics-informed indicator space, providing a scalable and interpretable foundation for dynamic response analysis. Building on this foundation, a hierarchical DRPP optimization framework is further developed to achieve the coordinated siting of dynamic reactive power resources. The main contributions are as follows:

1) A transient response indicator set is developed to capture key dynamic behaviors of RCS.

2) An EPCM-based method reconstructs ECC controllability within an interpretable indicator space, forming stability-oriented response matrices that preserve dominant control features.

3) A scalable DRPP optimization framework is established, integrating system controllability, local support and multi-device synergy into a unified decision model.

Comprehensive simulation studies demonstrate that the proposed siting strategy achieves the most effective configuration under limited compensation capacity, significantly mitigating transient overvoltage and post-fault oscillations.

II. Framework Design

A. Architecture Overview

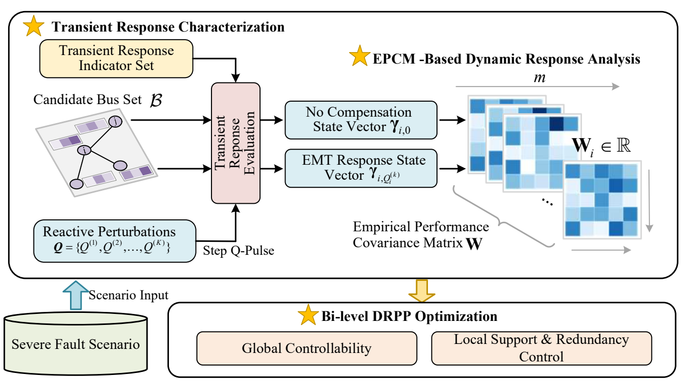

Fig. 1. Architecture of the EPCM-Based DRPP.

Fig. 1 presents the architecture of the proposed framework. The methodology consists of these functional layers:

1) **Transient Response Characterization:** A set of transient response indicators is proposed to quantify key voltage and power recovery features, providing interpretable and physical descriptors of system stability.

2) **EPCM-based Dynamic Response Analysis:** Based on the defined indicator set, the EPCM is formulated to approximate the controllability features of the traditional ECC within the indicator space. This formulation preserves the dominant spectral characteristics of system dynamics while emphasizing stability-relevant behaviors, resulting in a stability-oriented response representation.

3) **Bi-level DRPP Optimization:** EPCM-derived metrics are embedded into a bi-level model for dynamic reactive power planning. The upper level maximize global voltage controllability and ensure balanced systemwide response. The lower level strengthens local weak-bus support and coordinates multi-device interactions to enhance synergy and limit redundancy.

This framework serves as the foundation for the subsequent sections: Section III elaborates on the theoretical formulation of EPCM, while Section IV details the DRPP optimization model and algorithmic implementation.

B. Transient Response Evaluation Indicators

To comprehensively evaluate transient voltage and power responses in RCS, four indicators are defined. Let $v_i(t)$ and $P_i(t)$ denote the instantaneous voltage magnitude and active power at bus i, respectively. The fault occurs at t_f and clear at t_c, with T_b representing the integration duration. v_i^{ref} and P_i^{ref} are the pre-fault steady-state voltage and active power without compensation, while v^{rated} and P^{rated} denote the rated voltages and active power, respectively. Voltage thresholds for moderate and severe overvoltage are denoted by $v^{\max}$ and v^{crit}, and the range $[v_{\min}, v_{\max}]$ defines the acceptable steady-state voltage band. k_1 and k_2 are penalty coefficients satisfying $k_2 > k_1 > 0$. The function $\phi(x) = \eta_x \ln\big(1 + e^{(x-\delta_x)/\eta_x}\big)$ is a softplus operator ensuring smooth monotonic differentiability, where $\eta_x > 0$ controls the smoothness and δ_x denotes the tolerance threshold.

(1) **Overvoltage Severity Index (OVSI)**
Measures the duration and intensity of voltage excursions beyond specified thresholds.

$$\begin{aligned}\text{OVSI}_i^{\text{soft}} = \frac{1}{T_b}\int_{t_f}^{T_{\text{end}}} \Big[& k_1\,\phi\big(v_i(t) - v^{\max}\big) \\ & + k_2\,\phi\big(v_i(t) - v^{\text{crit}}\big)\Big]\mathrm{d}t,\end{aligned} \tag{1}$$

(2) **Voltage Recovery Energy (VRE)**
Quantifies voltage deviation energy during post-fault recovery.

$$\text{VRE}_i = \frac{1}{T_b}\int_{t_c}^{T_{\text{end}}} \left(\frac{v_i(t) - v_i^{\text{ref}}}{v^{\text{rated}}}\right)^2 \mathrm{d}t. \tag{2}$$

(3) **Active Power Fluctuation Energy (APFE)**
Measures the overall deviation of active power from its reference during transients, indicating oscillation intensity.

$$\text{APFE}_i = \frac{1}{T_b}\int_{t_c}^{T_{\text{end}}} \left(\frac{P_i(t) - P_i^{\text{ref}}}{P_i^{\text{rated}}}\right)^2 \mathrm{d}t. \tag{3}$$

(4) **Power Recovery Time Index (PRTI)**
Evaluates the speed and smoothness of active power recovery after fault clearance.

$$\text{PRTI}_i = \frac{1}{T_b}\int_{t_c}^{T_{\text{end}}} \phi\Bigg(\sqrt{\left(\frac{P_i(t) - P_i^{\text{ref}}}{P_i^{\text{rated}}}\right)^2 + \varepsilon^2}\Bigg)\,\mathrm{d}t, \tag{4}$$

III. EPCM-Based Dynamic Response Analysis

A. Theoretical Basis of Indicator-Space ECC Approximation

ECC originates from the controllability Gramian [10] and represents the time integral of the input–state covariance. It serves as a model-free indicator for evaluating controllability in nonlinear, high-dimensional power systems via eigenvalue analysis of the covariance matrix. However, conventional ECC

979-8-3315-8138-1

relies on full time-domain state trajectories, leading to excessive data volume and redundant information in large-scale RCS.

To overcome this limitation, this study introduces an *indicator-space approximation* of ECC, termed the EPCM. By replacing full state trajectories with a compact set of physically interpretable transient performance indicators, EPCM reconstructs the controllability covariance spectrum in a low-dimensional, stability-oriented space while retaining the key spectral features of ECC.

EPCM can accurately approximate the spectral structure of ECC when the following conditions are satisfied:

1) Monotonic and differentiable mapping: Each transient performance index originates from system state trajectories and varies smoothly and monotonically with respect to input perturbations.
2) Low-rank system dynamics: The system response is dominated by a few critical buses, causing the high-dimensional ECC to exhibit a concentrated energy distribution along a principal direction that the indicators can capture.

Suppose trajectories as $\boldsymbol{x}$ and indicators as $\boldsymbol{\gamma}$. Under these assumptions, a first-order approximation yields

$$\Delta\boldsymbol{\gamma} \approx J_{x\to\gamma}\,\Delta\boldsymbol{x}, \tag{5}$$

where $J_{x\to\gamma}$ denotes the Jacobian of the index–state mapping. Consequently,

$$\mathrm{EPCM} \approx J_{x\to\gamma}\,\mathrm{ECC}\,J_{x\to\gamma}^{\top}, \tag{6}$$

indicating that EPCM preserves the principal subspace of ECC when $J_{x\to\gamma}$ is well conditioned.

B. Definition

For a candidate bus i, consider a set of reactive perturbations $Q_i^{(k)}$, where $Q_i^{(k)}$ is the k-th applied reactive power pulse. The corresponding normalized transient response and baseline response are denoted by $\boldsymbol{\gamma}i, Q_i^{(k)}$ and $\boldsymbol{\gamma}_{i,0}$, respectively. For dynamic compensators such as STATCOMs, $Q_i^{(k)}$ can be approximated as a step reactive power injection. For dynamic compensators such as STATCOMs, the post-fault reactive power injection $Q_i^{(k)}$ can be approximated as a step reactive power pulse. The empirical performance controllability matrix (EPCM) of bus i is then defined as

$$\mathbf{W}_i = \frac{1}{K}\sum_{k=1}^{K}(\boldsymbol{\gamma}_{i,Q_i^{(k)}} - \boldsymbol{\gamma}_{i,0})(\boldsymbol{\gamma}_{i,Q_i^{(k)}} - \boldsymbol{\gamma}_{i,0})^{\top} \tag{7}$$

The matrix $\mathbf{W}_i$ quantifies the sensitivity of system transient responses to reactive perturbations at bus i. Its diagonal elements represent the controllability energy of individual indicators, while the off-diagonal terms describe their coupling and correlation. Thus, $\mathbf{W}_i$ serves as an empirical measure of how reactive power injections from bus i influence the system's dynamic behavior

Depending on the scope of construction, $\mathbf{W}_i$ can be formulated in two forms derived from (7) by selecting different subsets of indicators:

$$\mathbf{W}i^{G} = \frac{1}{K}\sum_{k=1}^{K}\big(\boldsymbol{\Gamma}i, Q_i^{(k)} - \boldsymbol{\Gamma}i,0\big)\big(\boldsymbol{\Gamma}i, Q_i^{(k)} - \boldsymbol{\Gamma}i,0\big)^{\top} \tag{8}$$

$$\mathbf{W}_i^{(b)} = \frac{1}{K}\sum_{k=1}^{K}(\boldsymbol{\gamma}^{(b)}_{i,Q_i^{(k)}} - \boldsymbol{\gamma}^{(b)}_{i,0})(\boldsymbol{\gamma}^{(b)}_{i,Q_i^{(k)}} - \boldsymbol{\gamma}^{(b)}_{i,0})^{\top}. \tag{9}$$

Where, $\boldsymbol{\Gamma}i, Q_i^{(k)} \in \mathbb{R}^{N_{\mathrm{ind}}\times N_{\mathrm{bus}}}$ denotes the system-level response vector formed by stacking N_{ind} transient indicators from all N_{bus} buses, whereas $\boldsymbol{\gamma}i, Q_i^{(k)^{(b)}} \in \mathbb{R}^{N\mathrm{ind}}$ represents the indicator subset corresponding to bus b. Accordingly, the global EPCM $\mathbf{W}i^{G} \in \mathbb{R}^{(N_{\mathrm{ind}}N_{\mathrm{bus}})\times(N_{\mathrm{ind}}N_{\mathrm{bus}})}$ captures the system-wide controllability pattern of compensator i, while the local EPCM $\mathbf{W}i^{(b)} \in \mathbb{R}^{N_{\mathrm{ind}}\times N_{\mathrm{ind}}}$ quantifies its controllability energy and indicator coupling at bus b.

C. Response Modeling

Based on the defined EPCM structures, three quantitative metrics are established:

1) Global Controllability Balance. The global $\log\det(\mathbf{W}_i^{G})$ measures the controllability volume in the indicator space, where a larger value denotes broader and more balanced system excitation, implying stronger overall controllability.
2) Local Controllability Energy. The trace of the local EPCM, $\mathrm{tr}(\mathbf{W}_i^{(b)})$ measures the controllability energy of compensator i at bus b, reflecting its capability to enhance local voltage recovery and damping.
3) Dynamic Response Mode Similarity. To assess redundancy among compensators, the pairwise similarity between buses i and j is calculated using the normalized Frobenius inner product:

$$\Phi_{ij} = \frac{\langle \mathbf{W}_i^{G}, \mathbf{W}_j^{G}\rangle_F}{\|\mathbf{W}_i^{G}\|_F\,\|\mathbf{W}_j^{G}\|_F}, \tag{10}$$

where $\langle\cdot,\cdot\rangle_F$ denotes the Frobenius inner product. The average similarity index is then defined as

$$\overline{\Phi} = \frac{2}{g(g-1)}\sum_{i<j} z_i z_j \Phi_{ij}, \tag{11}$$

where $z_i \in \{0,1\}$ indicates whether compensator i is selected and $g = \sum_i z_i$ is the number of selected compensators. A smaller $\overline{\Phi}$ implies greater diversity in response modes, indicating more complementary and less redundant voltage control actions.

Together, these metrics describe the global controllability volume, local controllability energy, and coordination redundancy, forming a unified basis for the hierarchical optimization framework introduced in the next section.

IV. DRPP Optimization and Implementation

This section presents the DRPP optimization framework based on the EPCM. The objective is to determine the optimal siting of dynamic reactive power compensators, such as STATCOMs, to enhance voltage controllability and support weak buses in the RCS. Both the upper and lower optimization levels are formulated by minimizing the negative form of their respective objectives: the upper level minimizes the negative log-determinant of the aggregated EPCM to maximize global controllability, while the lower level minimizes the negative trace term to strengthen local support and mitigate redundancy. This bi-level framework jointly integrates global controllability

979-8-3315-8138-1

Algorithm 1: EPCM-Based DRPP Optimization

Require: Candidate bus set $\mathcal{B} = \{1, 2, \dots, m\}$; reactive perturbations $\{Q_k\}_{k=1}^{K}$; number of devices g; tolerances $(\varepsilon_d, \varepsilon_{\mathrm{red}})$; weak-bus projector $\mathbf{M}$; severe fault χ_s.

Ensure: Optimal siting vector $\boldsymbol{z}^* \in \{0,1\}^m$.

Step 1: EPCM Construction For each $i \in \mathcal{B}$ and fault scenario χ_s, perform EMT Q-pulse simulations with $\{Q_k\}$ to obtain $\boldsymbol{\gamma}_{i,Q_k}$. Compute $\mathbf{W}_i$ as (8)(9).

Step 2: Bi-Level Optimization Solve the bi-level optimization problem as described in (12)–(13) using NOMAD.

Step 3: EMT Validation Deploy the optimal siting vector $\boldsymbol{z}^*$ in the EMT model, apply benchmark faults, and compare the transient indicators before and after compensation.

enhancement and local coordination, providing a systematic approach to redundancy suppression and weak-bus voltage support. The optimization procedure is structured as follows:

A. Upper-Level Optimization (Global Controllability)

The upper-level optimization aims to maximize the overall system controllability by selecting an optimal and non-redundant set of compensation buses. It employs the *global controllability balance metric* $\log\det(\mathbf{W})$ to enlarge the controllability volume in the high-dimensional indicator space, ensuring that the selected g compensators contribute well-dispersed dynamic responses.

$$\min_{\boldsymbol{z}\in\{0,1\}^m} \; -\log\det\Big(\sum_{i\in\mathcal{B}} z_i\, \mathbf{W}_i^{\mathrm{G}}\Big), \text{s.t.} \quad \sum_{i\in\mathcal{B}} z_i = g \tag{12}$$

Where m denotes the total number of candidate buses. $\boldsymbol{z}$ is the binary siting vector, and $\mathcal{B}$ represents the candidate bus set. Each $\mathbf{W}_i^{\mathrm{G}} \in \mathbb{R}^{(NL)\times(NL)}$ is the *global EPCM* of bus i, obtained by stacking all L transient indicators from all N nodes, thereby capturing the system-wide controllability structure.

B. Lower-Level Optimization (Local Support and Redundancy Coordination)

The lower-level optimization refines the siting solution by improving voltage support at weak buses and mitigating redundancy among compensators. It maximizes the *local controllability energy* $\mathrm{tr}(\mathbf{W})$ within the subset of weak buses $\mathcal{B}_{\mathrm{weak}}$, while constraining both the *global controllability balance* and the *response similarity index* $\overline{\Phi}$ defined earlier.

Each $\mathbf{W}_i^{(b)} \in \mathbb{R}^{L\times L}$ denotes the *local EPCM* of bus b under compensation at candidate bus i, derived from the variations of its L transient indicators. This localized representation isolates how each compensator affects the dynamic indicators of an individual node.

$$\begin{aligned} \min_{\boldsymbol{z}\in\{0,1\}^m} \; & -\sum_{b\in\mathcal{B}_w} \alpha_b\, \mathrm{tr}\Big(\sum_{i\in\mathcal{B}} z_i \mathbf{W}_i^{(b)}\Big) \\ \text{s.t.} \;\; & \mathrm{logdet}\Big(\sum_{i\in\mathcal{B}} z_i \mathbf{W}_i^{\mathrm{G}}\Big) \ge (1-\varepsilon_d)\, \mathrm{logdet}\Big(\sum_{i\in\mathcal{B}} z_i^* \mathbf{W}_i^{\mathrm{G}}\Big), \\ & \overline{\Phi} \le \varepsilon_{\mathrm{red}}. \end{aligned} \tag{13}$$

Where the first constraint maintains global controllability within $(1-\varepsilon_d)$ of the upper-level optimum, while the second limits similarity among selected compensators. z_i^* denotes the optimal siting solution obtained from the upper-level optimization.

The two layers jointly balance controllability volume and energy to enhance global and local voltage dynamics. The DRPP Optimization procedure is shown in Algorithm 1.

V. Case Study

A. Test System

The experimental system, depicted in Fig. 2, comprises five PV aggregated units, collectively providing a total capacity of 16 GW. The sending-end VSC-HVDC converter station is designed with a transmission capacity of 10 GW and a rated voltage of ±800 kV. In this system, the severe fault scenario is a double-phase-to-ground fault on line #7-#8 near bus #7.

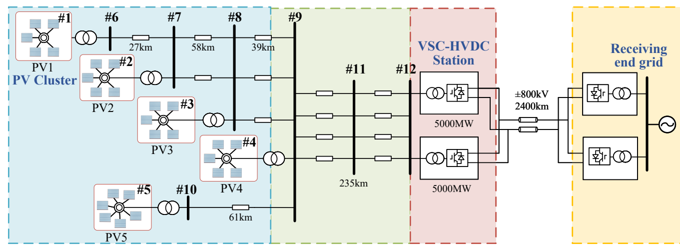

Fig. 2. System architecture diagram.

B. EPCM Construction

The 220 kV buses (#1–#5) of the PV clusters and the 500 kV backbone buses (#6–#11) are selected as candidate locations for dynamic reactive power compensation devices. Step reactive perturbations, denoted by $\{Q_k\}_{k=1}^{K}$, are applied to these candidate buses with magnitudes of 50, 100, 200, 300, 400, and 500 Mvar. The corresponding system responses are recorded and utilized to construct the EPCM.

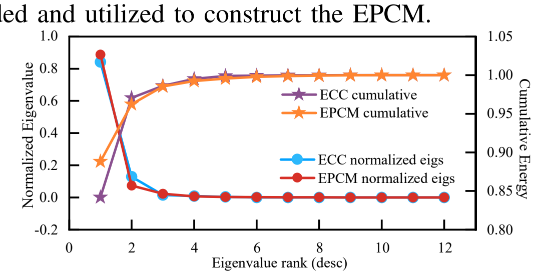

Fig. 3. Spectral energy comparison between ECC and EPCM.

To verify that the EPCM preserves the controllability spectrum of ECC in the indicator space, the normalized eigenvalue distribution and cumulative spectral energy of the aggregated matrices $\sum_i \mathbf{W}i^{\mathrm{ECC}}$ and $\sum_i \mathbf{W}i^{\mathrm{EPCM}}$ are compared, as shown in Fig. 3. Each eigenvalue is normalized as $E_k = \lambda_k / \sum_j \lambda_j$, and the cumulative energy ratio is $E\mathrm{cum}(r) = \sum k = 1^r \lambda_k / \sum_j \lambda_j$. The close agreement of both spectra confirms that the EPCM effectively retains the dominant controllability modes and spectral energy characteristics of the original ECC.

C. Comparison on Siting Performance

To comprehensively evaluate the siting performance of the proposed method, comparative simulations are conducted with three representative benchmarks, including the ECC, the static voltage sensitivity index (SVSI), voltage stiffness (VS) [11], and the dynamic voltage sensitivity index (DVSI) [10]. All methods are tested under different numbers of compensators as $g \in \{1, 3, 4\}$, to investigate their scalability and sensitivity

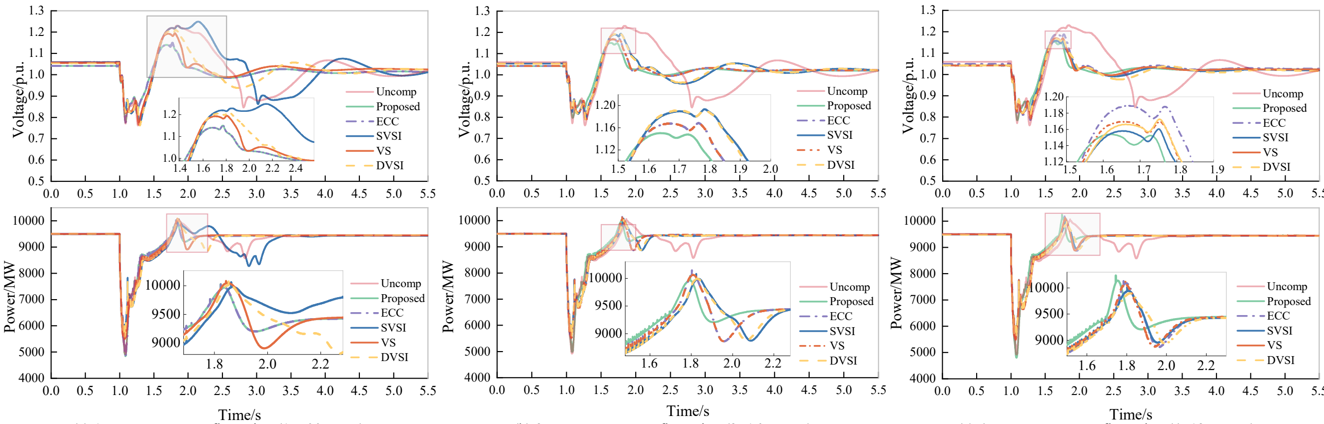

(a) 1 compensator configuration (1×500 Mvar) (b) 3 compensators configuration (3×167 Mvar) (c) 4 compensators configuration (4×125 Mvar)

Fig. 4. Transient response comparison of DRPP and benchmark methods (total capacity = 500 Mvar).

to installation scale. Table I presents the optimal placement combinations of compensators obtained from the proposed optimization framework under different comparison methods.

TABLE I
OPTIMAL PLACEMENT (BUS INDICES) UNDER DIFFERENT METHODS.

g	Proposed (EPCM-Bi)	ECC	VS	SVSI	DVSI
1	5	5	1	11	5
3	1, 4, 5	1, 2, 5	1, 2, 5	4, 9, 11	4, 5, 11
4	2, 5, 6, 7	1, 2, 3, 5	1, 2, 5, 6	2, 4, 9, 11	3, 4, 5, 11

As shown in Fig. 4, the proposed DRPP consistently outperforms benchmark methods, exhibiting faster voltage recovery, lower overvoltage peaks, smaller post-fault oscillations, and smoother active-power restoration. In the single-compensator case (Fig. 4(a)), the EPCM reproduces the controllability characteristics of the ECC. With additional compensators (Fig. 4(b)–(c)), the DRPP achieves complementary siting configurations and markedly improved transient stability compared with the ECC-based results.

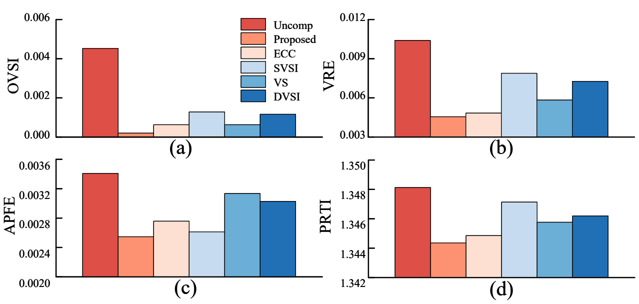

Fig. 5. Spectral energy comparison between ECC and EPCM.

To further evaluate system-level performance improvement, Fig. 5 presents the average values of the four transient indicators across all buses under $g = 3$. The proposed DRPP method achieves the lowest overall scores in OVSI, VRE, APFE and PRTI, indicating faster voltage recovery, smaller oscillation energy, and smoother power restoration. These results demonstrate that the proposed hierarchical siting strategy effectively enhances both global and local dynamic voltage stability compared with ECC and conventional sensitivity-based methods.

CONCLUSION

This paper proposed a unified EPCM-based framework for dynamic reactive power planning in RCSs. By introducing transient response indicators and reconstructing the ECC in an interpretable indicator space, the proposed method captures dominant controllability characteristics with reduced data dimensionality and improved physical interpretability. The formulated bi-level optimization integrates global controllability maximization and local redundancy coordination, enabling efficient and synergistic siting of dynamic var devices. Simulation results confirm that the EPCM-based DRPP significantly mitigates transient overvoltage, accelerates voltage recovery, and suppresses post-fault oscillations under severe disturbances. Future work will extend this framework toward capacity optimization and DRPP under multi-scenario uncertainty.

REFERENCES

[1] W. Wang, G. Li and J. Guo, "Large-scale renewable energy transmission by HVDC: Challenges and proposals," *Engineering*, vol. 19, pp. 252–267, Dec. 2022.

[2] P. Meng, W. Xiang, Y. Chi, Z. Wang, W. Lin and J. Wen, "Resilient DC voltage control for islanded wind farms integration using cascaded hybrid HVDC system," *IEEE Trans. Power Syst.*, vol. 37, no. 2, pp. 1054–1066, Mar. 2022.

[3] F. Blaabjerg, Y. Yang, K. A. Kim, and J. Rodriguez, "Power electronics technology for large-scale renewable energy generation," *Proc. IEEE*, vol. 111, no. 4, pp. 335–355, Apr. 2023.

[4] L. Yu, S. Xu, H. Sun, B. Zhao, G. Wu and X. Zhou, "Multiple renewable short-circuit ratio for assessing weak system strength with inverter-based resources," *CSEE J. Power Energy Syst.*, vol. 10, no. 6, pp. 2271–2282, Nov. 2024.

[5] Y. Zhang, N. Wiese, Z. Liu and M. Braun, "On the control interaction of synchronous machine and inverter-based resources during system-split situations," *Int. J. Electr. Power Energy Syst.*, vol. 152, p. 109227, Oct. 2023.

[6] S. Liao, Z. Li and D. Gan, "A study on transient overvoltage caused by HVDC tie blocking in multi-rectifier systems," *Int. J. Electr. Power Energy Syst.*, vol. 153, p. 109402, Nov. 2023.

[7] J. E. Suarez Patiño, L. A. Gallego Pareja and O. Gómez Carmona, "Optimal placement, sizing and operation of D-STATCOMs in power distribution systems using a mixed-integer linear programming model," *Results Eng.*, vol. 26, p. 104749, June 2025.

[8] S. Wildenhues, J. L. Rueda and I. Erlich, "Optimal allocation and sizing of dynamic var sources using heuristic optimization," *IEEE Trans. Power Syst.*, vol. 30, no. 5, pp. 2538–2546, Sept. 2015.

[9] Y. Chi, Y. Xu and R. Zhang, "Many-objective robust optimization for dynamic var planning to enhance voltage stability of a wind-energy power system," *IEEE Trans. Power Del.*, vol. 36, no. 1, pp. 30–42, Feb. 2021.

[10] J. Qi, W. Huang, K. Sun and W. Kang, "Optimal placement of dynamic var sources by using empirical controllability covariance," *IEEE Trans. Power Syst.*, vol. 32, no. 1, pp. 240–249, Jan. 2017.

[11] G. Wang, Y. Huang and Z. Xu, "Voltage stiffness for strength evaluation of VSC-penetrated power systems," *IEEE Trans. Power Syst.*, vol. 39, no. 4, pp. 6119–6122, July 2024.

979-8-3315-8138-1